

Novel Reactive Thermoplastic Resin as a Matrix for Laminates Containing Phase Change Microcapsules

Giulia Fredi , Andrea Dorigato, Alessandro Pegoretti

Department of Industrial Engineering and INSTM Research Unit, University of Trento, Trento, Italy

This work aims at developing multifunctional thermoplastic laminates combining structural and heat storage/management functions. The laminates are constituted by paraffin microcapsules as phase change materials (PCM), continuous carbon fibers, and a novel thermoplastic liquid methyl methacrylate resin (Elium), processable as a thermoset. The characterization aims to study how the paraffin microcapsules influence the thermo-mechanical properties and thermal management performance of Elium and of the relative composite laminates. For the Elium/PCM systems, the phase change enthalpy increased with the experimental PCM concentration up to 101 J/g, but the mechanical properties decreased concurrently. The melting enthalpy of the laminates also increased with the microcapsule amount, up to 66.8 J/g, which indicates that the mild conditions applied in the processing of the liquid resin allow the integrity of the microcapsules to be preserved. This is also confirmed by the improved thermal management performance observed through thermal camera imaging measurements. Microscopy techniques showed that the PCM phase is preferentially distributed in the interlaminar region, which accounts for the observed decrease in the interlaminar strength and the flexural properties with an increase in the PCM content. These results show a potential for the future development of multifunctional thermoplastic composites with elevated thermal energy storage capabilities. POLYM. COMPOS., 40:3711–3724, 2019. © 2019 Society of Plastics Engineers

INTRODUCTION

Organic phase change materials (PCMs) are nowadays the most widely used materials for thermal energy storage (TES), especially in the low-medium temperature range (0°C–100°C) [1]. They represent an innovative, renewable and clean energy technology that can improve the heat storage/release efficiency and the thermal management in many applications [1–5]. Since organic PCMs can store a considerable amount of latent heat at a nearly constant temperature, their use is remarkably advantageous for the accumulation of waste or excess thermal energy for a later use. Possible

applications include solar–thermal power plants and waste industrial heat recovery [6, 7], but also thermal management aimed at maintaining the indoor temperature in the human comfort range [8–10] or at avoiding overheating of electronic devices [11–17]. This PCM class, comprising paraffins, poly(ethylene glycol)s, and fatty acids, has several other advantages over the other TES materials, such as the small volume change upon phase change, the negligible supercooling, and the low density. Moreover, they are largely available, relatively cheap, chemically stable, non-corrosive, and easy to handle [3, 18, 19]. On the other hand, they need to be confined to avoid leakage above their melting temperature [20]. This can be addressed either by encapsulation in macro-, micro-, or nano-shells [21–23], or by shape-stabilization within a polymer matrix [24–28], a layered/porous structure [29, 30], or a nanofiller network [31–33]. Among these techniques, the microencapsulation is arguably the most diffused, as the shell tolerates volume change during the phase transition of the core and protects the PCM from the environment [21, 34].

In most of the applications, the heat storage/management system is just a supplementary module that is added to the main structure of a device, but the subsequent increase in weight and volume can be unacceptable for some applications. Therefore, it would be advantageous to embed the thermal storage function directly in the structural components, by producing multifunctional materials. In this perspective, polymer composites appear to offer wide possibilities for multifunctionality [35]. Lightweight composites featuring good mechanical properties and thermal management capability could be successfully applied in the automotive field, portable electronics industry, and smart technical garments sectors, where the weight saving is important but also the heat regulation and temperature management play a fundamental role [36].

In a polymer composite, the matrix can be a thermoplastic or a thermosetting polymer. Although the thermosetting (e.g., epoxy-based) composites generally feature higher mechanical properties, the thermoplastic composites have many other advantages, as they can be more easily recycled, post-thermoformed, welded, and repaired. Moreover, they are generally less expensive, need shorter processing time, and exhibit higher toughness and impact resistance [37].

Correspondence to: G. Fredi; e-mail: giulia.fredi@unitn.it; and A. Pegoretti; e-mail: alessandro.pegoretti@unitn.it
DOI 10.1002/pc.25233

Published online in Wiley Online Library (wileyonlinelibrary.com).

© 2019 Society of Plastics Engineers

On the other hand, thermoplastic polymers must be processed in the molten state, which complicates the processing of continuous fiber composites due to the high temperature required and the high melt viscosity [38], thereby hindering a wide diffusion of thermoplastic structural composites. A possible way to overcome these problems is to use a liquid thermoplastic resin that can be processed at room temperature. There are several examples in the literature of reactive processing of thermoplastic polymers such as polyamide, polyurethane and also poly(methyl methacrylate), but they still require medium–high or high temperatures during casting [39–41]. Conversely, the newly developed reactive methyl methacrylate matrix Elium can be processed at room temperature with processing techniques typical of thermosets, like resin transfer molding (RTM) and resin infusion, as the initial viscosity is as low as 100 mPa s (as reported in the technical datasheet). Unlike many thermoplastics, the mechanical properties of this resin are comparable to those of a high-performance epoxy resin [42], and it has been observed to feature even better vibration damping properties [39] and a higher fracture toughness [43], as well as a good adhesion strength with carbon fibers [44] and a low viscosity, which eases the processability [45]. Moreover, the interface created with glass fibers can be optimized by a proper acrylic sizing [46].

The scientific literature reports many examples of thermoplastic or thermosetting matrices containing microencapsulated or shape-stabilized PCMs [9, 18, 28, 47–52], which is a signal of the increasing interest of the scientific community for this topic. However, no studies are available on the influence of PCM microcapsules on the processability and the thermo-mechanical properties of a reactive thermoplastic matrix. Nevertheless, Elium/PCM systems could be interesting in the perspective of producing thermoplastic, post-thermoformable composites for thermal energy storage, and management. Moreover, the production process used to produce Elium-based components is particularly suitable to embed PCM microcapsules, as the low viscosity and the mild processing conditions are characterized by low shear stresses which help in preserving the integrity of the encapsulated PCM. Moreover, Elium/PCM systems are also suitable as matrices for multifunctional, high performance composites reinforced with continuous fibers. Even though this is an interesting research field with many potential applications, little research has been carried out so far to produce such multifunctional composites. Wirtz et al. [29] prepared a sandwich composite containing shape-stabilized paraffin for the temperature control of electronic devices, while Yoo et al. [53, 54] developed and characterized glass/epoxy laminates containing paraffin microcapsules. Recently, our group prepared epoxy/carbon laminates containing paraffin shape-stabilized with carbon nanotubes (CNTs) [52, 55], polyamide/glass laminates containing a microencapsulated and a shape-stabilized PCM [56, 57], and two types of semi-structural short carbon fibers composites including paraffin microcapsules, based on a thermoplastic (polyamide 12) [58] or a thermosetting (epoxy) [59] matrix, respectively. The

results of this wide-ranging experimental campaign suggested that (a) the microencapsulation is effective in preventing leakage when the PCM is processed with a polymer matrix, and (b) although thermoplastic composites show potential in this field, the severe processing conditions for thermoplastics can compromise the capsule shell integrity.

The aim of this work is to develop a novel thermoplastic laminate combining structural and TES function, constituted by a carbon fiber fabric, paraffin microcapsules, and a reactive thermoplastic matrix. The first part of the experimental activity is focused on the effect of the paraffin microcapsules on the thermal and mechanical properties of the resin. In the second part, the Elium/PCM mixtures were used as matrices in a hand lay-up process to produce carbon-fiber laminates whose mechanical and thermal properties were investigated along with their ability to store and release thermal energy.

MATERIALS AND METHODS

Materials

The three constituents of the produced laminates were a thermoplastic matrix, a paraffinic PCM and a carbon fabric-based reinforcement. The employed matrix was Elium 150, kindly provided by Arkema (Lacq, France). As mentioned before, Elium 150 is a thermoplastic, liquid, acrylic-based resin (reactive liquid methyl-methacrylate) [39], with a low viscosity at room temperature (100 mPa s). Water-free benzoyl peroxide (BPO) with 50% active content was provided together with the resin as a polymerization initiator. The selected PCM was the Microtek MPCM43D, purchased by Microtek Laboratories Inc. (Dayton, OH). In this system, the PCM phase was a paraffin wax, with a melting temperature of 43 °C, encapsulated in a melamine-formaldehyde based shell that constitutes approximately the 10% of the total capsules mass. The microcapsules (denoted as MC) presented an average diameter of 17–20 μm, and the melting enthalpy declared by the producer was 190–200 J/g. The carbon fiber fabric GG200P was purchased from G. Angeloni S.r.l. (Venice, Italy). It was a balanced plain weave carbon fabric (mass per unit area 192 g/m²), made of intermediate modulus carbon fibers (3,000 fibers per tow, linear density = 200 tex). All the materials were used as received.

Sample Preparation

Elium resin and BPO were manually mixed at room temperature in a weight ratio of 98:2 until the BPO was completely dissolved. The paraffin microcapsules were then added to the matrix in different weight concentrations (20, 30, and 40 wt% of the total weight of the mixtures) and mechanically stirred at 200 rpm for 5 min, to ensure a good dispersion. The mixtures were then degassed and poured in rectangular silicon molds with dimensions of 70 × 10 × 3 mm³, to produce specimens for the subsequent

mechanical and thermal characterization. After 4 h at room temperature, the mixtures were treated for 8 h at 80°C, to complete the polymerization process. The nomenclature and the nominal composition of the prepared samples are reported in Table 1.

The same compositions described before were also used as matrices to prepare laminates. The laminates were produced through a hand lay-up method. Five plies of carbon fabric were stacked together, and the resulting laminates had an in-plane area of 13 × 20 mm². The laminates were vacuum-bagged for 4 h at room temperature and thermally treated at 80°C for 8 h, to apply the same thermal cycle adopted for the matrices. A neat carbon fiber/Elium laminate without microcapsules was also prepared for comparison.

Characterization

Characterization of the Matrices. The microstructural properties of the prepared matrices were investigated through scanning electron microscopy (SEM). The specimens were cryofractured in liquid nitrogen and the fracture surface was investigated with a field-emission SEM Zeiss (Oberkochen, Germany) Supra 60, after Pt-Pd sputtering.

Differential scanning calorimetry (DSC) tests were performed with a Mettler (Columbus, OH) DSC30 calorimeter, between 0°C and 130°C, at a heating/cooling rate of 10°C/min, under a nitrogen flow of 100 ml/min. All the specimens (~20 mg each) underwent a first heating scan, a cooling scan and a second heating scan. The test allowed the measurement of the melting and crystallization temperatures (T_m , T_c) and the phase change enthalpy values (ΔH_m , ΔH_c) of the PCM, and the glass transition temperature (T_g) of the resin.

Thermogravimetric analysis (TGA) was performed with a Mettler (Columbus, OH) TG50 instrument on specimens of approximately 25 mg. The tests were performed at a heating rate of 10°C/min up to 700°C, under a nitrogen flow of 150 ml/min. The tests allowed the determination of the temperatures corresponding to a mass loss of 1 wt% ($T_{1\%}$), 3 wt% ($T_{3\%}$), and 5 wt% ($T_{5\%}$), the temperature at the maximum degradation rate (T_d), taken at the peak of the mass loss derivative signal, and the residual mass after the test (m_r).

TABLE 1. List of the prepared matrices with nominal composition, mass loss after sample preparation, and experimental capsule weight fraction.

Sample name	Nom. EL content (wt%)	Nom. MC content (wt%)	Exp. mass loss (wt%)	Exp. MC content (wt%)
EL	100.0	–	33.3 ± 3.3	–
EL-MC20	80.0	20.0	20.9 ± 1.9	25.3 ± 0.6
EL-MC30	70.0	30.0	18.6 ± 2.8	36.9 ± 1.2
EL-MC40	60.0	40.0	16.6 ± 0.7	48.0 ± 0.4

EL = Elium resin + benzoyl peroxide (2 wt%); MC = microcapsules.
nom. = nominal; exp. = experimental.

Dynamic mechanical thermal analysis (DMTA) was performed with a TA (New Castle, DE) Q800DMA instrument in single cantilever bending mode. The specimens had nominal dimensions of 35 × 10 × 3 mm³ and the distance between the grips was fixed at 17.5 mm. Storage modulus (E') and loss tangent ($\tan\delta$) were measured between 0°C and 180°C at a heating rate of 3°C/min, with a strain amplitude of 0.05% and a frequency of 1 Hz.

Three-point bending tests were performed according to ASTM D790-03 standard, with an Instron (Norwood, MA) 5,969 universal testing machine, equipped with a 50 kN load cell. The nominal dimensions of the tested specimens were 70 × 10 × 3 mm³. The span length was 50 mm and the crosshead speed was fixed at 1.5 mm/min. The tangent modulus of elasticity (E), the flexural strength (σ_{FM}), and the flexural strain at break (ϵ_b) were determined for each specimen according to Eqs. 1–3:

$$E = (L^3 m) / (4bd^3) \quad (1)$$

$$\sigma_{FM} = (3PL) / (2bd^2) \quad (2)$$

$$\epsilon_b = (6Dd) / (L^2) \quad (3)$$

where L is the support span, m is the slope of the tangent to the initial portion of the load-deflection curve, b and d are the specimen width and thickness, P is the maximum load, and D is the deflection at the break point.

Characterization of the Laminates. The mass fraction of the matrix (resin + microcapsules) for each laminate was calculated by subtracting the mass of the fibers, which is known from the area of the laminate and the mass per unit area of the fabric, from the total weight of the laminate. The fiber-to-matrix mass ratio obtained in this way was compared with that measured through TGA. The experimental density of the laminates was measured with a displacement method in ethanol, through a Gibertini E42 analytical balance. After obtaining the theoretical and experimental densities of the laminates, the volume fraction of the components and the porosity were determined, as already described in our previous article [57].

Optical microscope (OM) images were obtained on polished cross sections at different magnification levels, through an upright incident-light optical microscope Zeiss (Oberkochen, Germany) Axiophot featuring Epiplan Neo-fluar objectives. Scanning electron microscopy (SEM) micrographs of the cryofractured surfaces of all the laminates were acquired through a field-emission SEM Zeiss Supra 60, after Pt–Pd sputtering. This technique allowed the investigation of both the delamination plane and the cross section of the laminates.

DSC and TGA tests were performed in the same experimental conditions utilized for the matrices. DMTA tests were performed as described for the matrices on samples with nominal in-plane area of 35 × 5 mm² and the thickness

of each laminate. Two specimens were tested for each composition, to ensure consistency of results.

To check the overall thermal management capacity of the laminates, a simple test was performed with a thermal camera. Rectangular specimens with a surface area of $90 \times 120 \text{ mm}^2$ were heated in an oven at 60°C for 30 min, then removed and left cooling down to room temperature under laboratory conditions. During the cooling phase, the surface temperature was recorded with an infrared thermal imaging camera (FLIR E60, placed at a fixed position at a distance of 30 cm from the laminate surface).

Three-point flexural tests were performed with the same equipment used to test the matrices. The nominal in-plane dimensions of the tested specimens were $120 \times 10 \text{ mm}^2$, and the thickness was that of each laminate. The specimens were cut out of the prepared laminates with a diamond wheel. The span length was 85 mm and the crosshead speed was fixed at 9 mm/min. At least five specimens were tested for each sample. The tangent modulus of elasticity (E) and the flexural strain at break (ϵ_b) were determined in the same way as reported for the matrices (Eqs. 1 and 3), while the flexural strength (σ_{FM}) was determined with Eq. 4 as:

$$\sigma_{\text{FM}} = \frac{3PL}{2bd^2} \left[1 + 6 \left(\frac{D}{L} \right)^2 - 4 \left(\frac{D}{L} \right) \left(\frac{d}{L} \right) \right] \quad (4)$$

to consider the not negligible forces developed at the supports derived by a high span-to-thickness ratio, as the ASTM D790 standard suggests. It should be mentioned that this equation is based on the assumption of a linear stress distribution through the specimen thickness, which is not fully correct for laminates. However, the results are still useful for comparison purposes [60].

RESULTS AND DISCUSSION

Characterization of the Matrices

As mentioned before, Table 1 reports the sample designation with the nominal compositions; the nominal weight fraction of MC was 20, 30, or 40 wt%. However, a sensible mass loss was observed during the sample preparation. This was due to the evaporation of the most volatile fraction of the resin, as suggested by the sensible temperature decrease of Elium/MC mixtures during mixing. From the initial (just after casting) and final (after the thermal treatment) masses of the samples, the mass loss was measured for each sample and reported in Table 1. From these data, the experimental MC weight fraction was recalculated, and the values reported in Table 1.

Fig. 1a–d reports the SEM micrographs of the cryofracture surface of the prepared samples. From the fracture surface of the sample EL-MC20 at low magnifications (Fig. 1a), it can be observed that the capsules are homogeneously distributed within the polymer matrix. This was

also assessed through SEM micrographs acquired at even lower magnifications, not reported here for the sake of brevity. Some capsules are broken, which is likely due to the cryofracturing process and not because of the applied processing conditions, which were rather mild. The core-shell structure of the microcapsules is clearly visible, especially in the micrograph acquired at higher magnifications (Fig. 1b). In the microcapsule indicated with a solid red arrow, both the thin polymer shell and the paraffinic core are visible. The irregular shape and the voids of the core indicate a certain capability of the capsules to accommodate the volume expansion during the phase change and avoid the shell damage [61]. In other cases (dashed black arrow), a portion of the shell is visible, but the core was almost completely removed. The fracture propagation mostly occurring across the capsules and not at the interface suggests a rather good adhesion with the polymer matrix [62]. However, from a comparison between the sample EL-MC20 (Fig. 1b) and the sample with the highest MC concentration (EL-MC40, Fig. 1c), it is evident that in this latter case the number of broken capsules is considerably reduced, which also reinforces the hypothesis that the processing conditions do not remarkably damage the microcapsules. In the case of EL-MC40 (Fig. 1c and d), the fracture propagates at the resin–MC interface and probably follows the path of the defectiveness and voids in the polymer matrix. In this case, the volume fraction of Elium is not sufficient to allow a proper wettability of all the capsules, with a consequent high level of porosity.

Fig. 2 reports the DSC thermograms of the first heating scan and the cooling scan of the prepared matrices, while the most important results of the DSC analysis are summarized in Table 2, where also the data of the neat MC are reported for comparison. The thermograms of all the samples containing microcapsules show an endothermic peak at 45°C – 49°C , which corresponds to the melting of the PCM contained in the microcapsules, and an exothermic peak at 25°C – 30°C indicating the crystallization phenomenon. From the data of Table 2 it can be observed that the melting and crystallization temperatures are respectively higher and lower than those measured on the neat MC sample, which is probably due to inertial phenomena during the DSC tests. The intensity of these peaks increases with the MC weight fraction. From the peak areas, the experimental values of the melting and crystallization enthalpy were calculated and reported in Table 2 as $\Delta H_{\text{m,exp}}$ and $\Delta H_{\text{c,exp}}$, respectively. These values are in good agreement with the expected values ($\Delta H_{\text{m,theor}}$ and $\Delta H_{\text{c,theor}}$) calculated from the experimental weight fraction reported in Table 1 and the experimental melting and crystallization enthalpy values of the neat MC, which implies that the adopted production process preserves the capsule integrity. The DSC data allow also the measurement of the glass transition (T_g) of the resin; it can be observed that the values are not remarkably different from that of the neat Elium sample (EL), which suggests that the presence of microcapsules does not interfere with the polymerization

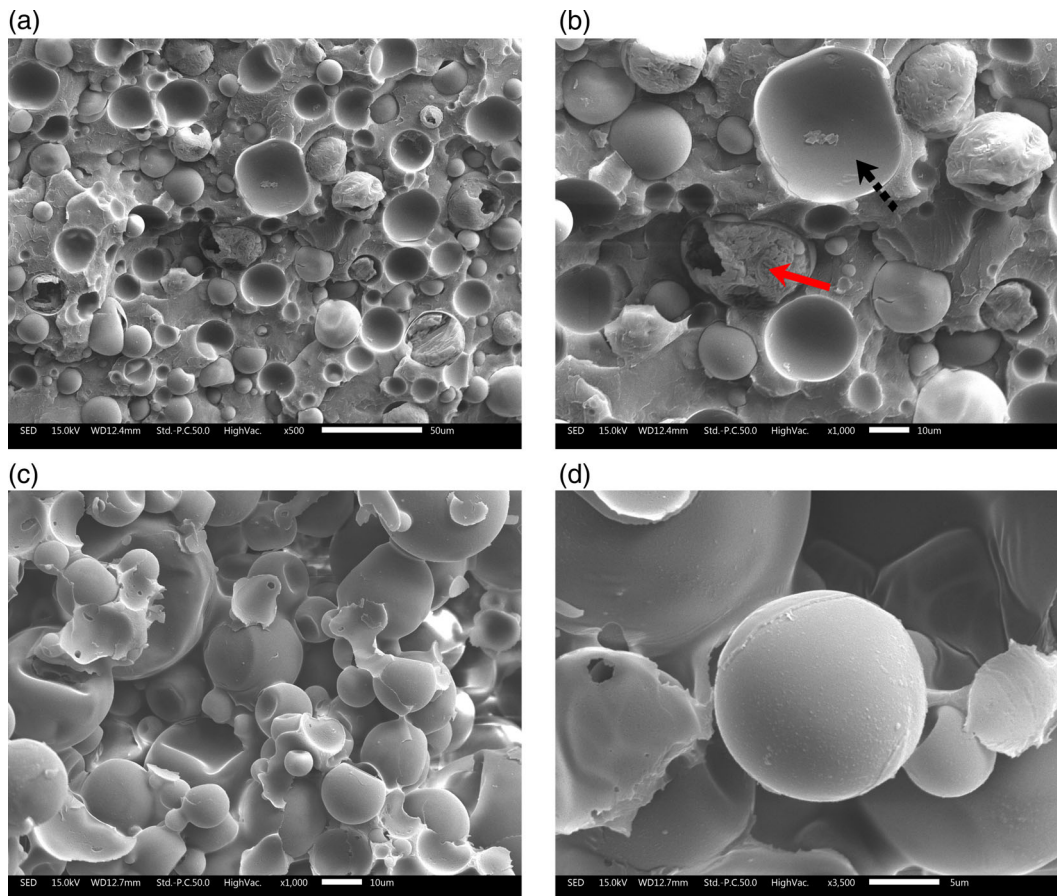


FIG. 1. SEM micrographs of the cryofracture surface of some selected compositions: (a) EL-MC20 (0.5 kX); (b) EL-MC20 (1 kX). Solid (dotted) arrow indicates microcapsule where the paraffinic core is still (not anymore) present; (c) EL-MC40 (1 kX); and (d) EL-MC40 (3.5 kX). [Color figure can be viewed at wileyonlinelibrary.com]

process. The same behavior was also observed in our previous work on epoxy/microcapsules matrices [52]. The T_g measured in the second heating scan, not reported here for the sake of brevity, never differs from that of the first

heating scan for more than 2°C – 3°C , which implies that the applied thermal cycle was suitable to complete the polymerization process.

Fig. 3a–b reports the thermograms obtained from the TGA tests, and Table 3 collects the most important parameters detected from TGA. The EL sample degrades in a single step at approximately 415°C , while the neat MC show a higher peak degradation temperature ($\sim 466^\circ\text{C}$) and a broader degradation temperature interval. However, the degradation temperatures of the two phases are not different enough to allow the presence of two distinct degradation steps in the mass-versus-temperature thermogram (Fig. 3a), thereby limiting the possibility of calculating an experimental MC weight fraction. However, in the mass loss derivative signal (Fig. 3b), the degradation of the two phases is observable through in two distinct peaks. The height of the peak at lower temperature, associated to the degradation of EL, decreases with an increase in the MC weight fraction, while the peak related to the MC degradation follows the opposite trend. This is why the values of T_d , determined as the maximum in the mass loss derivative signal, increase with an increase in the MC weight fraction.

The results of the DMTA tests are reported in Fig. 4a and b and in Table 4. Fig. 4a reports the trend of the storage

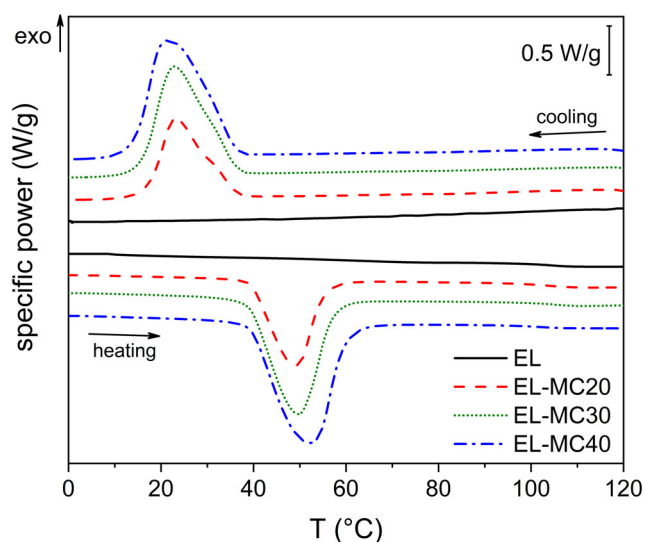


FIG. 2. DSC thermograms of the samples EL-MC x ($x = 20, 30, 40$). [Color figure can be viewed at wileyonlinelibrary.com]

TABLE 2. Results of the DSC tests of the samples EL, EL-MC x ($x = 20, 30, 40$) and MC.

	T_g (°C)	T_m (°C)	$\Delta H_{m,exp}$ (J/g)	$\Delta H_{m,theor}$ (J/g)	T_c (°C)	$\Delta H_{c,exp}$ (J/g)
EL	103.6	—	—	—	—	—
EL-MC20	103.8	47.0	53.1	52.6 ± 1.3	25.0	53.5
EL-MC30	104.6	47.7	80.8	76.7 ± 2.5	24.8	81.6
EL-MC40	101.7	49.9	101.4	99.8 ± 0.8	23.7	100.1
MC	—	45.0	208.2	—	29.8	208.2

T_g = glass transition temperature of Elium; T_m , T_c = melting and crystallization temperatures of the PCM; $\Delta H_{m,exp}$, $\Delta H_{c,exp}$ = experimental melting and crystallization enthalpies of the PCM; $\Delta H_{m,theor}$ = theoretical melting enthalpy of the PCM calculated from the measured capsule weight fraction MC (exp. wt%).

modulus (E') normalized to the E' value of the same sample at 0°C. For the neat EL sample, the storage modulus decreases with an increase in temperature; the decrease happens with a slower rate up to 60°C and with a higher slope above this temperature. In the samples containing MC, E' decreases with a higher rate up to 50°C–60°C due to the PCM melting, and the normalized value of E' at 60°C decreases with an increase in the MC weight

fraction, as also observable from the data in Table 4. On the $\tan\delta$ thermograms (Fig. 4b), two peaks are visible. The first at 40°C–50°C is associated to the PCM melting; it is interesting to note that not only the peak height but also the peak temperature increases with an increase in the MC content. These signals and trends open possibilities to use DMTA to study the melting/crystallization phenomena of PCM once embedded in the polymer matrix, which is quite unusual in the field of polymers and composites. Further analysis is in progress to have a better comprehension of these phenomena [63]. The second peak at 115°C–125°C is related to the glass transition of the polymer matrix, and also the position of this peak increases with an increase in the MC weight fraction, probably because the capsule shells contribute to limit the polymer chain mobility. It is worth noting that also the residual storage modulus E'_R , measured at 160°C, increases with an increase in the capsule weight fraction, probably still due to the contribution of the microcapsules in limiting the chain mobility, as observed for other thermoplastic composites [63].

The influence of the microcapsules on the mechanical properties was evaluated through three-point bending test. Fig. 5a shows representative load–displacement curves, while the main results of the test are reported in Fig. 5b. The elastic modulus decreases with an increase in the MC weight fraction, and the lowest value (i.e., 1.35 ± 0.18 GPa) is measured on the sample EL-MC40, with a decrease of 35% with respect to the elastic modulus of the neat EL, equal to 2.08 ± 0.25 GPa. This effect can be reasonably explained by assuming that the MC's are probably less stiff than the neat resin. More dramatic is the decrease in the flexural strength, which decreases from 63 MPa of the neat EL down

 TABLE 3. Results of the TGA tests on the samples EL, MC and EL-MC x ($x = 20, 30, 40$).

Sample	$T_{1\%}$ (°C)	$T_{3\%}$ (°C)	$T_{5\%}$ (°C)	T_d (°C)	m_r (%)
EL	221.7	279.1	301.7	415.0	0
EL-MC20	208.3	275.0	295.0	416.2	0.35
EL-MC30	201.7	240.2	281.7	420.3	1.10
EL-MC40	188.3	228.3	268.3	455.2	2.09
MC	186.3	235.0	298.7	466.2	2.67

$T_{1\%}$, $T_{3\%}$, $T_{5\%}$ = temperature corresponding to a mass loss of 1%, 3%, 5%; T_d = temperature of the maximum degradation kinetics (peak of the mass loss derivative); m_r = residual mass.

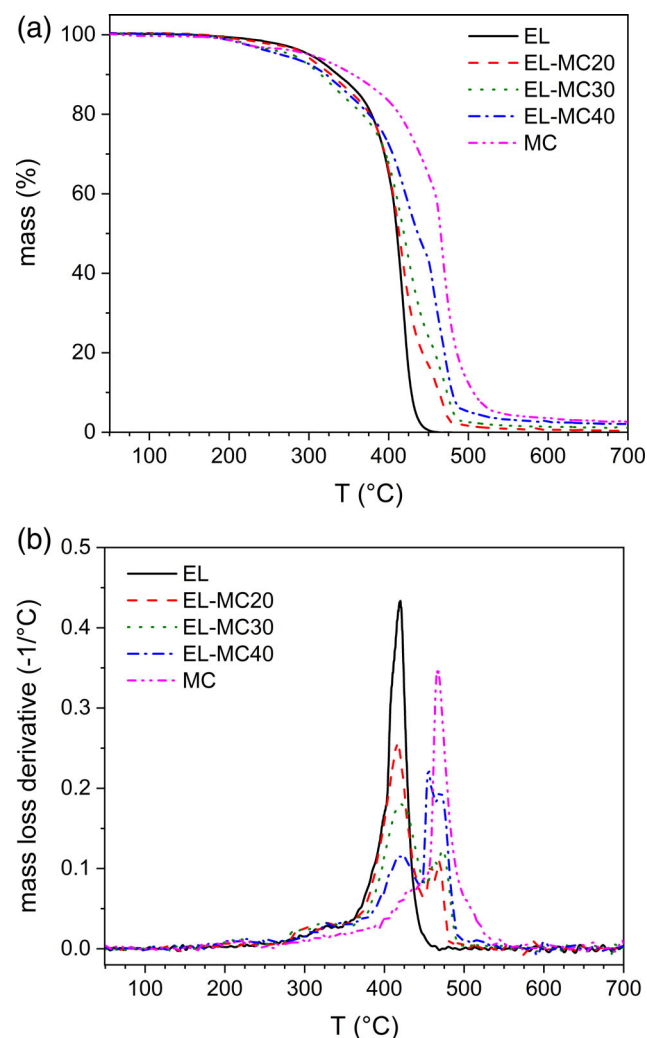


FIG. 3. TGA thermograms of the samples EL, EL-MC x ($x = 20, 30, 40$) and MC. (a) Residual mass; and (b) mass loss derivative. [Color figure can be viewed at wileyonlinelibrary.com]

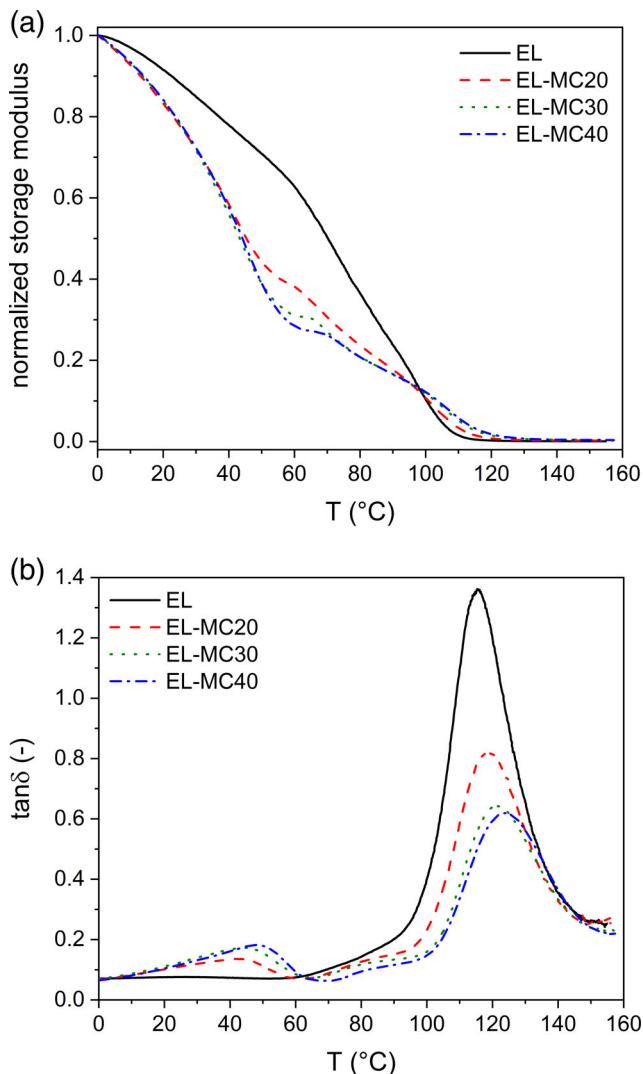


FIG. 4. DMTA results on the samples EL and EL-MC x ($x = 20, 30, 40$). (a) Normalized storage modulus; and (b) loss tangent ($\tan\delta$). [Color figure can be viewed at wileyonlinelibrary.com]

to 17 MPa of the sample EL-MC40, with a decrease of 73%. This is probably associated to the lower strength of the MC and the non-optimal adhesion of the capsules with the polymer matrix. On the other hand, the strain at break is not heavily affected by the presence of MC, as the values of ϵ_b of the four compositions are not significantly different from

TABLE 4. Main results of the DMTA tests on the samples EL and EL-MC x ($x = 20, 30, 40$).

Sample	$T_{m,peak}$ (°C)	$T_{g,peak}$ (°C)	$E'_{60^\circ C}/E'_{0^\circ C}$ (-)	E'_R (MPa)
EL	—	115.4	0.627	1.71
EL-MC20	42.1	119.1	0.382	5.49
EL-MC30	44.2	121.8	0.311	8.37
EL-MC40	47.9	124.2	0.284	10.03

$T_{m,peak}$ = peak of $\tan\delta$ in correspondence of the PCM melting; $T_{g,peak}$ = peak of $\tan\delta$ in correspondence of the glass transition of Elium. E'_R = residual storage modulus at 160°C.

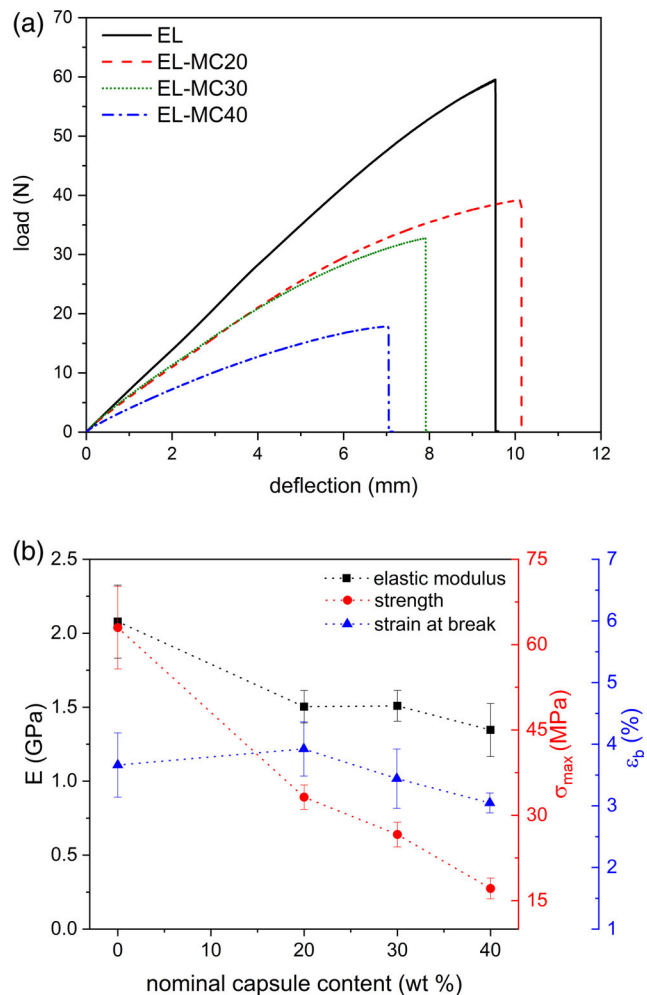


FIG. 5. Results of the three-point flexural test on the samples EL and EL-MC x ($x = 20, 30, 40$). (a) Representative load-deflection curves; and (b) elastic modulus, flexural stress, and strain at break as a function of the capsule content. [Color figure can be viewed at wileyonlinelibrary.com]

one another. Similar trends were observed in our previous works on PCM-containing polymer matrices [52, 56].

Characterization of the Laminates

Fig. 6a–f reports the optical microscope images of the polished cross sections of the prepared laminates. The core-shell structure of the microcapsules is evident also from these micrographs, especially at higher magnification level (Fig. 6f). It can be clearly seen that the PCM phase is preferentially distributed in the interlaminar zones and not among the fibers of the same tow, which depends on the different dimensions of carbon fibers (average diameter 7 μm) and microcapsules (average diameter 20 μm). This was observed also in our previous work, where the matrix was an epoxy resin and the PCM phase was constituted by paraffin shape-stabilized with carbon nanotubes [57]. However, in that case, the PCM domains were larger, had an irregular shape and caused a partial distortion of the fiber tows, which is not observed in the present case. Thus,

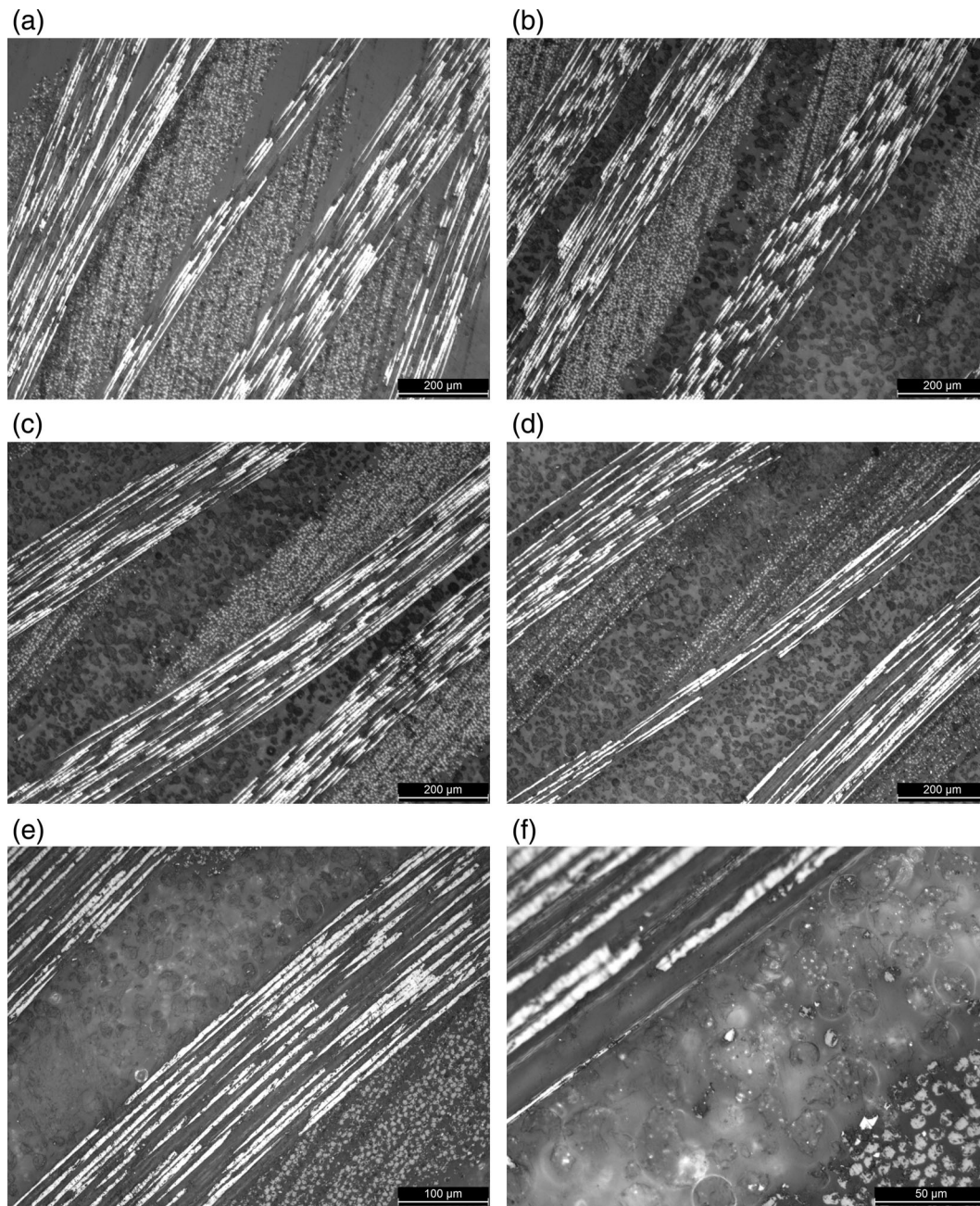


FIG. 6. Optical microscope images of the polished cross section of the prepared laminates (a) EL-CF; (b) EL-MC20-CF; (c) EL-MC30-CF; (d) EL-MC40-CF; (e) and (f) EL-MC30-CF at higher magnification.

a reduction in the size of the PCM phase is beneficial to preserve the shape and the original disposition of the fibers within the fabric. It can be also observed that the concentration of the paraffin capsules in the interlaminar region does not change remarkably with an increase in the MC weight fraction of the initial Elium-MC mixture. What is really resulting to change is the thickness of the interlaminar region, and thus that of the whole laminate, which increases with the MC fraction. The preferential location of the microcapsules in the interlaminar region is also visible from the SEM micrographs reported in Figure 7a–d. The delamination plane of the sample EL-MC30-CF (Fig. 7a

and b) shows the presence of microcapsules. Similar results were obtained also by Yoo et al. [53]. From the comparison between the cross-sections of the samples EL-CF (Fig. 7c) and EL-MC30-CF (Fig. 7d), it is evident that the interlaminar region of the latter is rich in MC, and its thickness increases when microcapsules are added.

The results of the DSC tests on the laminates are reported in Table 5. The DSC thermograms are not reported here for the sake of brevity, since they are qualitatively similar to those reported for the matrices (see Fig. 2). Also in the case of the laminates, the glass transition of the resin is practically not affected by the presence of the

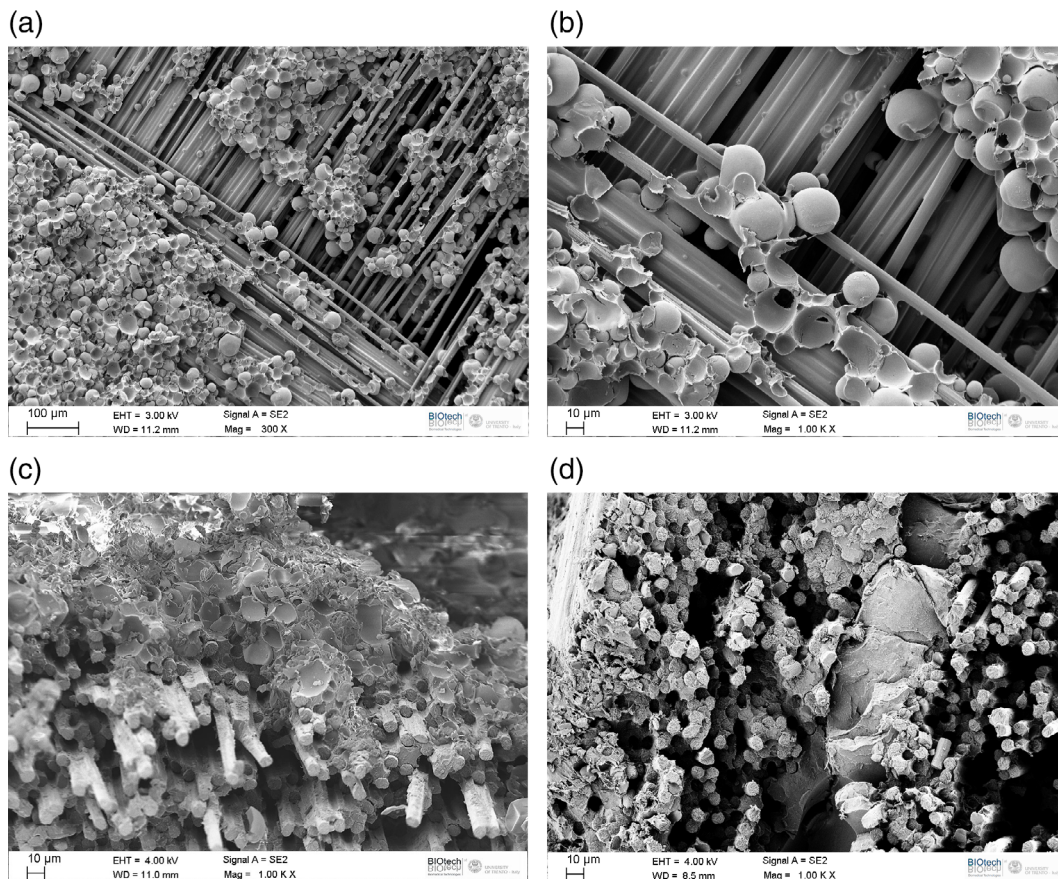


FIG. 7. SEM micrographs of the cryofracture surface of some selected compositions. (a) and (b) EL-MC30-CF, delamination plane; (c) EL-MC30-CF, cross section; and (d) EL-CF, cross section. [Color figure can be viewed at wileyonlinelibrary.com]

microcapsules, and it lies in the same temperature range as that of the matrices, which implies that the polymerization process is not influenced by the presence of both MC and CF. Again, the melting and crystallization temperatures of the PCM phase do not follow a specific trend with the MC concentration, but the values of T_m are generally lower than those of the matrices and the values of T_c generally higher, which can be due to the higher thermal conductivity imparted by the presence of carbon fibers. The melting and crystallization enthalpy values increase with the nominal MC content, up to 66.8 J/g for the sample EL-MC40-CF, which is considerably higher than any values obtained previously for laminates of the same kind, that is, composed of a polymer

matrix, a continuous fiber fabric reinforcement and a PCM, considering not only the work of our group [54, 56, 57]. This indicates that the Elium resin is suitable to preserve the heat storage ability of the embedded PCM.

In the preparation of the laminates, the experimental weight fraction of MC in the starting matrix mixtures was known, but the final MC weight fraction in the laminates also depends on the final matrix weight fraction, which for these laminates is influenced by the initial matrix viscosity that in turn depends on the starting MC loading. From the DSC tests, it is possible to calculate an experimental MC weight fraction from the measured melting enthalpy, assuming that the MC maintain their energy storage efficiency also when embedded in the

TABLE 5. Results of the DSC tests on the prepared laminates.

Sample	T_g (°C)	T_m (°C)	$\Delta H_{m,exp}$ (J/g)	T_c (°C)	$\Delta H_{c,exp}$ (J/g)	MC _{exp} (wt%)
EL-CF	101.0	—	—	—	—	—
EL-MC20-CF	102.5	46.6	30.23	27.5	31.6	14.5
EL-MC30-CF	99.6	45.3	45.9	29.5	45.6	22.1
EL-MC40-CF	98.6	46.4	66.8	27.4	65.6	32.1

T_g = glass transition temperature of Elium; T_m , T_c = melting and crystallization temperatures of the PCM; $\Delta H_{m,exp}$, $\Delta H_{c,exp}$ = experimental melting and crystallization enthalpies of the PCM; MC_{exp} = experimental capsule weight fraction calculated from the measured melting enthalpy.

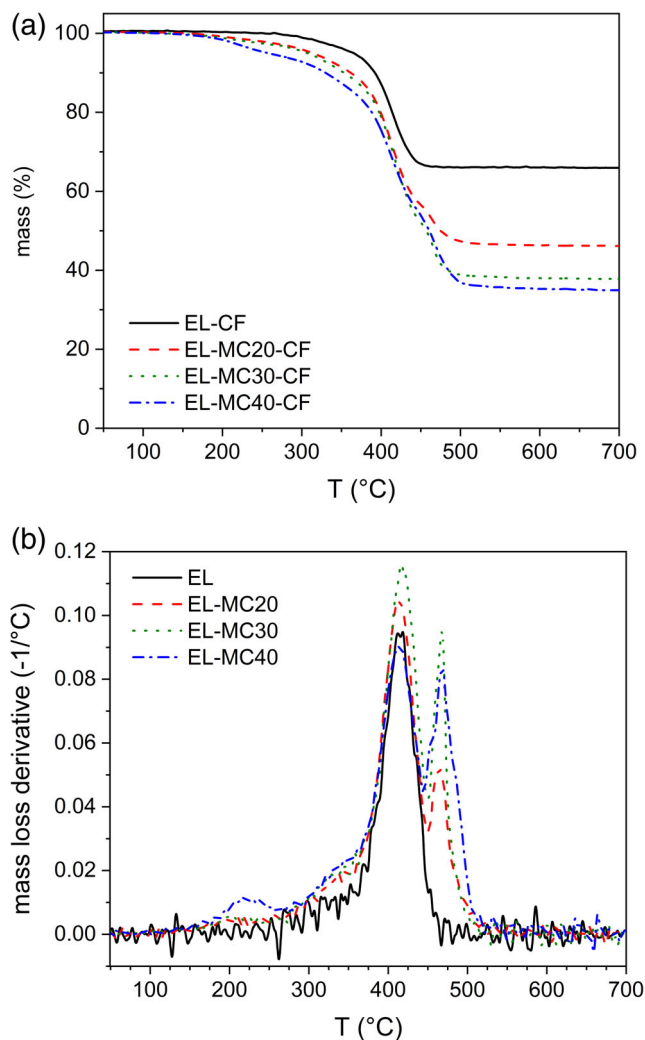


FIG. 8. TGA thermograms of the prepared laminates. (a) Residual mass; and (b) mass loss derivative. [Color figure can be viewed at wileyonlinelibrary.com]

laminates, which is a reasonable hypothesis considering the results of the characterization of the matrices. These data of experimental MC loading (MC_{exp}) are reported in Table 5.

TGA tests were performed to investigate the thermal stability of the laminates and to estimate the fiber weight fraction. The TGA thermograms are reported in Fig. 8a and b, while Table 6 collects the most important results. Both the trends of the residual mass (Fig. 8a) and the mass loss derivative (Fig. 8b) are qualitatively similar to those reported for the matrices (Fig. 3a and b). However, the residual mass (m_r) at

the end of the test is considerably higher for the laminates, due to the presence of carbon fibers. It can be noted that m_r decreases with an increase in the MC content, which implies that the matrix weight fraction increases with the MC loading. From these results, the fiber weight fraction was calculated for each laminate (CF_{TGA}), and the results are reported in Table 6. The CF weight fraction decreases when the MC loading increases, and ranges from 66 wt% for the neat laminate to 37 wt% for the sample EL-MC40-CF. It can be observed that this decrease is not linear with the MC weight fractions reported in Table 5. The weight fraction of fibers and matrix determined in this way is in good agreement with that determined by weighing the whole laminates and subtracting the weight of the fibers, as described in Paragraph 2.4.2, reported in Table 6 as CF_{mass} . This accordance is an indication of the homogeneity of the produced samples. The decreased CF weight fraction is probably the reason of the decreasing thermal stability of the laminates with an increase in the MC loading, as can be noted from the decreasing values of $T_{1\%}$, $T_{3\%}$, and $T_{5\%}$ in TGA tests. In any case, these temperatures are always higher than those measured on the matrices (Table 3), which highlights the positive contribution of the CF to the thermal stability of the laminates. The trends of the mass loss derivative as a function of temperature (Fig. 8b) still show two main degradation peaks representing the degradation of the resin and of the capsules, respectively. The position of these peaks is not influenced by the presence of carbon fibers, as it coincides with that measured on the matrices.

Table 7 shows the weight fraction of carbon fibers, determined as the average of CF_{TGA} and CF_{mass} , and of the microcapsules, determined through DSC. These data allowed the calculation of the theoretical density of the samples; from the experimental density obtained by the displacement method, the volume fraction of pores was calculated, and then the fiber and capsule volume fractions. It can be observed that the fiber volume fraction decreases with an increase in the MC content. This is due to the higher viscosity of the matrix, which does not easily flow out of the fabric during the vacuum bag process. It can be also observed that the porosity is around 2 vol % for all the samples except for EL-MC40-CF, in which the pore volume fraction rises to 5.2 vol%.

The results for the thermal imaging camera tests are reported in Fig. 9. As observed for epoxy/ CF laminates containing shape-stabilized paraffin [57], in the laminates containing the PCM, the temperature decreases with a

TABLE 6. Results of the TGA tests on the prepared laminates.

Sample	$T_{1\%}$ (°C)	$T_{3\%}$ (°C)	$T_{5\%}$ (°C)	T_d (°C)	m_r (%)	CF_{TGA} (wt%)	CF_{mass} (wt%)
EL-CF	301.7	335.0	361.7	416.3	65.9	65.9	67.8
EL-MC20-CF	210.5	281.7	315.0	415.0	48.5	48.3	47.8
EL-MC30-CF	195.0	268.3	308.3	420.3	37.7	37.1	40.7
EL-MC40-CF	188.3	235.0	281.7	413.6	38.2	36.9	39.5

$T_{1\%}$, $T_{3\%}$, $T_{5\%}$ = temperature corresponding to a mass loss of 1%, 3%, 5%; T_d = temperature of the maximum degradation kinetics (peak of the mass loss derivative); m_r = residual mass; CF_{TGA} = fiber weight fraction calculated from TGA residual masses; CF_{mass} = fiber weight fraction calculated from laminate weighing.

TABLE 7. Fiber content, experimental density, porosity, and thickness of the laminates.

Sample	CF ^a (wt%)	MC _{exp} (wt%)	ρ_{th} (g/cm ³)	ρ_{exp} (g/cm ³)	Porosity (vol%)	CF (vol%)	MC (vol%)
EL-CF	66.9 ± 1.4	0	1.511 ± 0.019	1.487 ± 0.013	1.6 ± 2.1	56.7 ± 1.6	0
EL-MC20-CF	48.1 ± 0.3	14.5	1.329 ± 0.005	1.300 ± 0.012	2.2 ± 1.3	35.6 ± 0.6	20.95 ± 0.19
EL-MC30-CF	38.9 ± 2.6	22.1	1.253 ± 0.036	1.238 ± 0.003	1.2 ± 3.2	27.4 ± 1.9	30.41 ± 0.07
EL-MC40-CF	38.2 ± 1.8	32.1	1.211 ± 0.026	1.148 ± 0.001	5.2 ± 2.4	25.0 ± 1.2	40.93 ± 0.04

^aaverage between CF_{TGA} and CF_{mass}, see Table 6.

different trend showing a pseudo-plateau caused by the release of latent heat during the crystallization process of the paraffin, while for the neat EL-CF laminate an exponential temperature decay is observed. Due to the heat released, the time to reach room temperature is noticeably increased. For example, the time required to reach 30°C is of about 3.5 min for the EL-CF composite and it increases up to about 20 min for the sample EL-MC40-CF. It should be pointed out that the cooling rate also depends on the mass of the laminate, which was not the same for the different laminates. However, the presence of plateaus in the temperature trend clearly highlights the differences in the thermal behavior of the laminates as a function of the MC content.

Fig. 10a and b shows the results of the DMTA test, in the plots the trends of the normalized storage modulus (E') and the loss tangent ($\tan\delta$) are represented as a function of temperature. This test allows the detection of all the thermal transitions of the tested specimens in the selected temperature range. The storage modulus (Fig. 10a) decreases in two main steps.; the first step at 45°C–50°C is associated to the paraffin melting, and the second, at 100°C–120°C, corresponds to the glass transition of the Elium matrix. The amplitude of the first step increases with the MC content. The $\tan\delta$ thermogram shows peaks in correspondence of the steps of E' . As in the case of the matrices (Fig. 4b), the

height and position of the peak associated to the PCM melting increase with the MC weight fraction.

The results of the three-point bending tests are reported in Fig. 11a and b. Fig. 11a shows representative load–displacement curves. As already observed for laminates containing CNT-stabilized paraffin [57], the curves of all the samples present an initial linear region that is followed by a region where the slope decreases until the maximum load is reached. After the maximum load, the neat laminate is

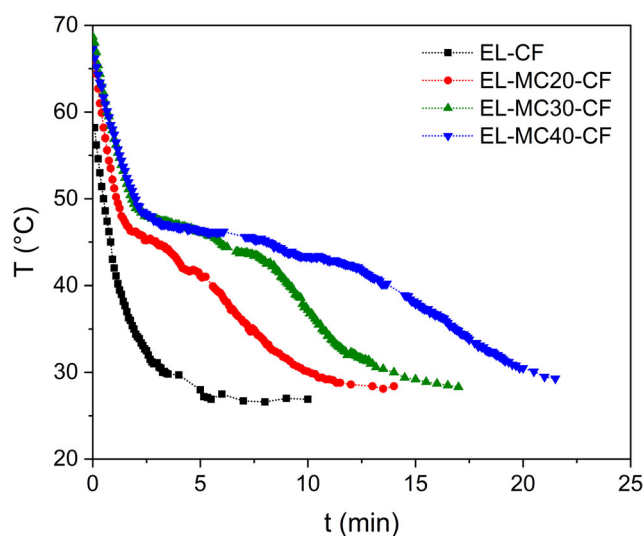


FIG. 9. Results of the thermal imaging camera tests on the prepared laminates. Surface temperature as a function of time. [Color figure can be viewed at wileyonlinelibrary.com]

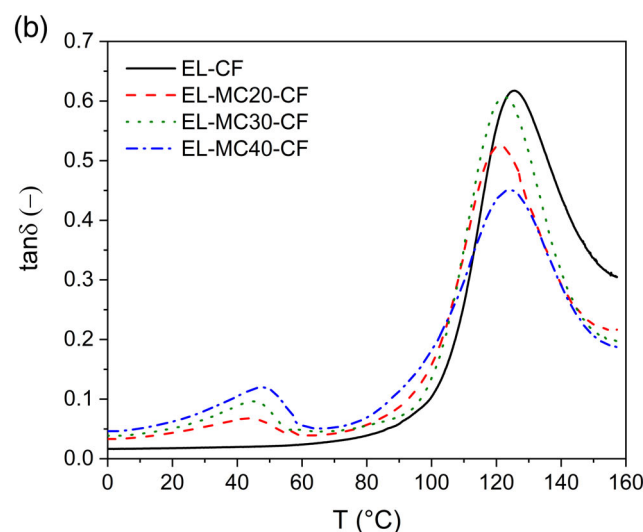
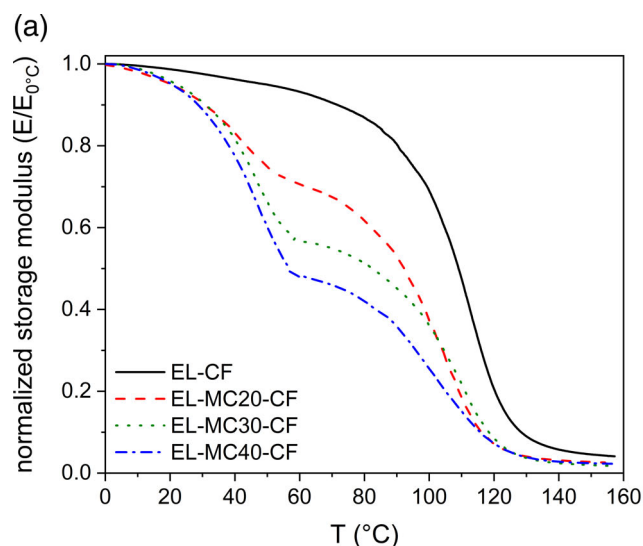


FIG. 10. Results of the DMTA test on the laminates. (a) Normalized storage modulus ($E'/E'_{0°C}$); and (b) $\tan\delta$. [Color figure can be viewed at wileyonlinelibrary.com]

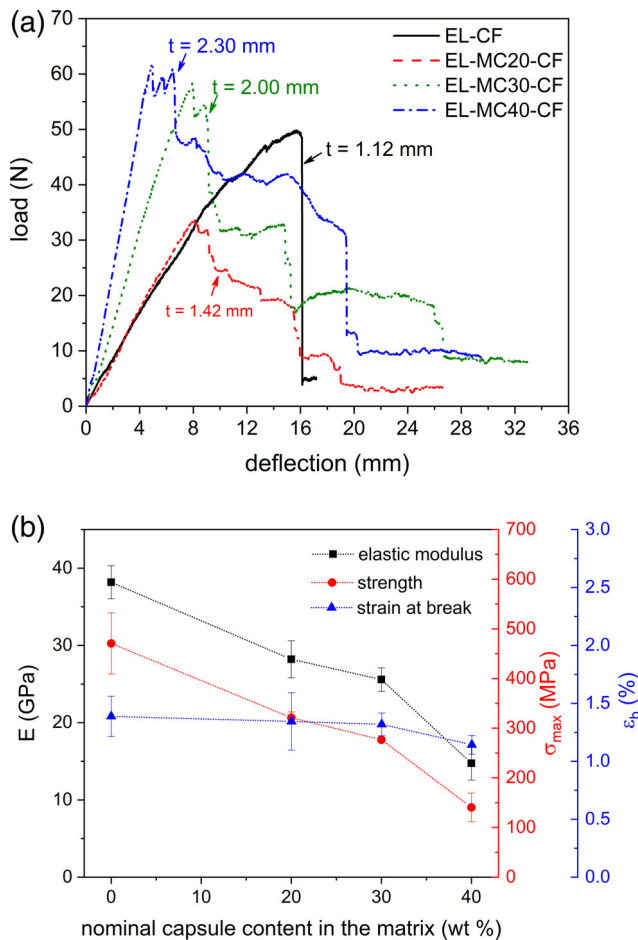


FIG. 11. Results of the three-point flexural tests on the laminates. (a) Representative load–deflection curves (t = thickness of the laminates). (b) Elastic modulus, flexural stress, and strain at break as a function of the capsule content. [Color figure can be viewed at wileyonlinelibrary.com]

subjected to a catastrophic failure, starting from the tensile-stressed mid-lower region of the specimen, which suggests a good interlaminar adhesion [64, 65]. Conversely, the samples EL-MC x -CF ($x = 20, 30, 40$) undergo a progressive failure and present a drop-plateau sequence in the load–displacement curve, thus absorbing mechanical energy also during damage propagation. The damage was observed starting either in the mid-upper zone, subjected to compression, or in one of the interlaminar regions. This failure mode, reported elsewhere for woven fabric composites [65], has been related to laminates with a tensile strength considerably higher than the interlaminar shear strength, which is likely the case for the MC-containing laminates reported in this work. The results of the three-point bending test are reported in Fig. 11b. The elastic modulus is seen decreasing with an increase in the MC content, but this is partially due to the decreasing fiber volume fraction. However, although the decrease is remarkable in the sample EL-MC40-CF, the elastic modulus of the sample EL-MC30-CF could still be considered acceptable for some applications. Moreover, the bending strength decreases with the MC loading, which is probably due to the presence of failure mechanisms such as delamination and failure in the

zone subjected to compression. In accordance with the results shown for the matrices, the flexural strain at break is not dramatically affected by the presence of MC.

CONCLUSIONS

For the first time, PCM microcapsules were embedded in the reactive thermoplastic Elium matrix, for the production of continuous carbon fiber laminates with TES capability. The first part of the work was devoted to study the effect of the paraffin microcapsules on the thermo-mechanical properties of the resin. Samples with different capsule weight fractions (20, 30, and 40 wt%) were prepared and characterized. The good heat storage/release capability of these systems was evidenced through DSC tests, where the measured phase change enthalpies were proportional to the experimental PCM content (i.e., up to 101 J/g for the sample EL-MC40). This indicates that the microcapsules retained all their TES properties, thanks to the mild production process of the Elium resin. SEM micrographs showed that the microcapsules were homogeneously distributed in the polymer matrix, with a non-optimal capsule/matrix interfacial adhesion. This effect, combined with the limited stiffness and strength of the microcapsules, was at the basis of the decrease in the elastic modulus and the flexural strength of the resin at elevated MC loadings. On the other hand, the elongation at break was not significantly affected by the PCM content. The viscoelastic properties of the resin were also affected by the presence of the PCM, as the storage modulus decreased with an increase in the PCM content and showed a step at the PCM melting, while the trend of the $\tan\delta$ presented a peak at the paraffin melting.

Elium/PCM compositions were employed as matrices to produce multifunctional thermoplastic laminates with heat storage/management function, containing various PCM weight fractions. The melting/crystallization enthalpy values increased with the capsule content, up to 66.8 J/g for the sample EL-MC40-CF. The considerably high phase change enthalpy was at the basis of the good thermal management performance, measured through thermal camera imaging. Microstructural analysis showed that the PCM phase was preferentially distributed in the interlaminar region, and that the laminate thickness increased with an increase in the capsule content, and so did the matrix (Elium/PCM) volume fraction, as also evidenced by TGA tests. These two effects were the main causes of the decrease in the mechanical properties of the laminates observed at elevated PCM contents. This suggests that the mechanical and TES properties do not work synergistically, and a compromise in the composition must be found according to the specific application. Nevertheless, the presented results show potential for the development of structural composites with TES capability. Future work will be focused on the improvement in the capsule-matrix adhesion, on the enhancement of the production process to increase the fiber volume fraction, and on an in-depth dynamic-mechanical

characterization of Elium-based laminates to assess how the PCM phase transition affects their viscoelastic properties.

ACKNOWLEDGMENTS

Dr. Pierre Gerard of Arkema (Lacq, France) is kindly acknowledged for the provision of Elium resin.

REFERENCES

1. K. Pielichowska and K. Pielichowski, *Prog. Mater. Sci.*, **65**, 67 (2014). <https://doi.org/10.1016/j.pmatsci.2014.03.005>.
2. J. Pereira da Cunha and P. Eames, *Appl. Energy*, **177**, 227 (2016). <https://doi.org/10.1016/j.apenergy.2016.05.097>.
3. A.S. Fleischer, *Thermal Energy Storage Using Phase Change Materials - Fundamentals and Applications*, Springer Briefs in Applied Science and Technology. Thermal Engineering and Applied Science, Minneapolis, MN (2015). <https://doi.org/10.1007/978-3-319-20922-7>.
4. B. Zalba, J.M. Marin, L.F. Cabeza, and H. Mehling, *Appl. Thermal Eng.*, **23**, 251 (2003). [https://doi.org/10.1016/S1359-4311\(02\)00192-8](https://doi.org/10.1016/S1359-4311(02)00192-8).
5. L.F. Cabeza, H. Mehling, S. Hiebler, and F. Ziegler, *Appl. Thermal Eng.*, **22**, 1141 (2002).
6. Z.Y. Wang, F. Qiu, W.S. Yang, and X.D. Zhao, *Renew. Sustain. Energy Rev.*, **52**, 645 (2015). <https://doi.org/10.1016/j.rser.2015.07.184>.
7. A.M. Khudhair and M.M. Farid, *Energ. Conver. Manage.*, **45**, 263 (2004). [https://doi.org/10.1016/S0196-8904\(03\)00131-6](https://doi.org/10.1016/S0196-8904(03)00131-6).
8. Y. Cui, J. Xie, J. Liu, and S. Pan, *Proc. Eng.*, **121**, 763 (2015). <https://doi.org/10.1016/j.proeng.2015.09.027>.
9. G. Kastiukas, X.M. Zhou, and J. Castro-Gomes, *Construct. Build Mater.*, **110**, 201 (2016). <https://doi.org/10.1016/j.conbuildmat.2016.02.029>.
10. K. Biswas, J. Lu, P. Soroushian, and S. Shrestha, *Appl. Energy*, **131**, 517 (2014). <https://doi.org/10.1016/j.apenergy.2014.02.047>.
11. S.C. Fok, W. Shen, and F.L. Tan, *Int. J. Thermal Sci.*, **49**, 109 (2010). <https://doi.org/10.1016/j.ijthermalsci.2009.06.011>.
12. F.L. Tan and C.P. Tso, *Appl. Thermal Eng.*, **24**, 159 (2004). <https://doi.org/10.1016/j.applthermaleng.2003.09.005>.
13. R. Kandasamy, X.-Q. Wang, and A.S. Mujumdar, *Appl. Thermal Eng.*, **27**, 2822 (2007). <https://doi.org/10.1016/j.applthermaleng.2006.12.013>.
14. S.K. Sahoo, M.K. Das, and P. Rath, *Renew. Sustain. Energy Rev.*, **59**, 550 (2016). <https://doi.org/10.1016/j.rser.2015.12.238>.
15. Y. Tomizawa, K. Sasaki, A. Kuroda, R. Takeda, and Y. Kaito, *Appl. Thermal Eng.*, **98**, 320 (2016). <https://doi.org/10.1016/j.applthermaleng.2015.12.056>.
16. L. Ianniciello, P.H. Biwolé, and P. Achard, *J. Power Sources*, **378**, 383 (2018). <https://doi.org/10.1016/j.jpowsour.2017.12.071>.
17. A. Lazrak, J.-F. Fourmigué, and J.-F. Robin, *Appl. Thermal Eng.*, **128**, 20 (2018). <https://doi.org/10.1016/j.applthermaleng.2017.08.172>.
18. P. Zhang, X. Xiao, and Z.W. Ma, *Appl. Energy*, **165**, 472 (2016). <https://doi.org/10.1016/j.apenergy.2015.12.043>.
19. A. Abhat, *Solar Energy*, **30**, 313 (1983). [https://doi.org/10.1016/0038-092X\(83\)90186-X](https://doi.org/10.1016/0038-092X(83)90186-X).
20. F. Agyenim, N. Hewitt, P. Eames, and M. Smyth, *Renew. Sustain. Energy Rev.*, **14**, 615 (2010). <https://doi.org/10.1016/j.rser.2009.10.015>.
21. T. Khadiran, M.Z. Hussein, Z. Zainal, and R. Rusli, *Sol. Energy Mater. Sol. Cells*, **143**, 78 (2015). <https://doi.org/10.1016/j.solmat.2015.06.039>.
22. E. Onder, N. Sarier, and E. Cimen, *Thermochim. Acta*, **467**, 63 (2008). <https://doi.org/10.1007/s12221-016-5113-z>.
23. J.-F. Su, X.-Y. Wang, S.-B. Wang, Y.-H. Zhao, K.-Y. Zhu, and X.-Y. Yuan, *Polym. Compos.*, **32**, 810 (2011). <https://doi.org/10.1002/pc.21102>.
24. P. Sobolciak, M. Karkri, M.A. Al-Maaded, and I. Krupa, *Renew. Energy*, **88**, 372 (2016). <https://doi.org/10.1016/j.renene.2015.11.056>.
25. M.L. Mu, P.A.M. Basheer, W. Sha, Y. Bai, and T. McNally, *Appl. Energy*, **162**, 68 (2016). <https://doi.org/10.1016/j.apenergy.2015.10.030>.
26. A.S. Luyt and I. Krupa, *Energ. Conver. Manage.*, **50**, 57 (2009). <https://doi.org/10.1016/j.enconman.2008.08.026>.
27. A. Sari, M. Akcay, M. Soylak, and A. Onal, *J. Sci. Ind. Res.*, **64**, 991 (2005).
28. A. Dorigato, M.V. Ciampolillo, A. Cataldi, M. Bersani, and A. Pegoretti, *Rubber Chem. Technol.*, **90**, 575 (2017). <https://doi.org/10.5254/rct.82.83719>.
29. Wirtz, R.; Fuchs, A.; Narla, V.; Shen, Y.; Zhao, T.; Jiang, Y., "Non-Metallic and Structurally Efficient Thermal Energy Storage Composites for Avionics Temperature Control, Part I: Thermal Characterization," in 42nd AIAA Aerospace Sciences Meeting and Exhibit, University of Nevada, Reno Reno, Nevada, pp 1 (2003).
30. P. Zhang, Y. Hu, L. Song, J. Ni, W. Xing, and J. Wang, *Sol. Energy Mater. Sol. Cells*, **94**, 360 (2010). <https://doi.org/10.1016/j.solmat.2009.10.014>.
31. A. Sari and M. Soylak, *J. Serb. Chem. Soc.*, **72**, 485 (2007). <https://doi.org/10.2298/jsc0705485s>.
32. A. Dorigato, P. Canclini, S.H. Unterberger, and A. Pegoretti, *Express Polym. Lett.*, **11**, 738 (2017). <https://doi.org/10.3144/expresspolymlett.2017.71>.
33. M. Mehrali, S.T. Latibari, M. Mehrali, T.M.I. Mahlia, and H. S.C. Metselaar, *Energ. Conver. Manage.*, **88**, 206 (2014). <https://doi.org/10.1016/j.enconman.2014.08.014>.
34. L. Bayés-García, L. Ventolà, R. Cordobilla, R. Benages, T. Calvet, and M.A. Cuevas-Diarte, *Sol. Energy Mater. Sol. Cells*, **94**, 1235 (2010). <https://doi.org/10.1016/j.solmat.2010.03.014>.
35. K. Friedrich. "Routes for Achieving Multifunctionality in Reinforced Polymers and Composite Structures," in *Multifunctionality of Polymer Composites: Challenges and New Solutions*, K. Friedrich and U. Breuer, Eds., Elsevier, Waltham, MA (2015, Chap. 1). <https://doi.org/10.1016/b978-0-323-26434-1.00001-5>.
36. W. Yuan, X. Yang, G. Zhang, and X. Li, *Appl. Thermal Eng.*, **144**, 551 (2018). <https://doi.org/10.1016/j.applthermaleng.2018.07.095>.
37. M. Biron, *Thermoplastics and Thermoplastic Composites*, Elsevier, Ltd, Waltham, MA (2013). <https://doi.org/10.1016/B978-1-4557-7898-0.00001-9>.

38. M. Nikforooz, J. Montesano, M. Golzar, and M.M. Shokrieh, *Polym. Test.*, **67**, 457 (2018). <https://doi.org/10.1016/j.polymertesting.2018.02.023>.
39. S.K. Bhudolia, P. Perrotey, and S.C. Joshi, *Compos. Struct.*, **179**, 502 (2017). <https://doi.org/10.1016/j.compstruct.2017.07.093>.
40. R.T. Durai Prabhakaran, *Mech. Adv. Mater. Struct.*, **21**, 213 (2013). <https://doi.org/10.1080/15376494.2013.834090>.
41. K. van Rijswijk, H.E.N. Bersee, A. Beukers, P.J. Picken, and A.A. van Geenen, *Polym. Test.*, **25**, 392 (2006). <https://doi.org/10.1016/j.polymertesting.2005.11.008>.
42. A. Chilali, W. Zouari, M. Assarar, H. Kebir, and R. Ayad, *J. Reinf. Plast. Compos.*, **35**, 1217 (2016). <https://doi.org/10.1177/0731684416645203>.
43. S.K. Bhudolia, P. Perrotey, and S.C. Joshi, *Compos. Part B Eng.*, **134**, 246 (2018). <https://doi.org/10.1016/j.compositesb.2017.09.057>.
44. T. Pini, F. Caimmi, F. Briatico-Vangosa, R. Frassine, and M. Rink, *Eng. Fract. Mech.*, **184**, 51 (2017). <https://doi.org/10.1016/j.engfracmech.2017.08.023>.
45. R. Muthuraj, Y. Grohens, and B. Seantier, *Nano-Struct. Nano-Objects*, **12**, 68 (2017). <https://doi.org/10.1016/j.nanoso.2017.09.002>.
46. Q. Charlier, F. Lortie, P. Gerard, and J. F. Gerard, "Interfacial Adhesion Between Glass Fibers and Acrylic-Based Matrices as Studied BY Micromechanical Testing," in 20th International Conference on Composite Materials, Copenhagen, July 19–24 (2015).
47. D. Rigotti, A. Dorigato, and A. Pegoretti, *Mater. Today Commun.*, **15**, 228 (2018). <https://doi.org/10.1016/j.mtcomm.2018.03.009>.
48. K. Resch-Fauster, F. Hengstberger, C. Zauner, and S. Holper, *Eng. Buildings*, **169**, 254 (2018). <https://doi.org/10.1016/j.enbuild.2018.03.068>.
49. K. Resch-Fauster and M. Feuchter, *Thermochim. Acta*, **663**, 34 (2018). <https://doi.org/10.1016/j.tca.2018.03.004>.
50. Y. Wu, C. Chen, Y. Jia, J. Wu, Y. Huang, and L. Wang, *Appl. Energy*, **210**, 167 (2018). <https://doi.org/10.1016/j.apenergy.2017.11.001>.
51. S.-G. Jeong, S. Kim, and W. Huh, *J. Adhes. Sci. Technol.*, **28**, 711 (2014). <https://doi.org/10.1080/01694243.2013.865331>.
52. G. Fredi, A. Dorigato, L. Fambri, and A. Pegoretti, *Polymers*, **9**, 405 (2017). <https://doi.org/10.3390/polym9090405>.
53. S. Yoo, E. Kandare, R. Shanks, M.A. Al-Maadeed, and A. Afaghi Khatibi, *Thermochim. Acta*, **642**, 25 (2016). <https://doi.org/10.1016/j.tca.2016.09.003>.
54. S. Yoo, E. Kandare, G. Mahendrarajah, M.A. Al-Maadeed, and A.A. Khatibi, *J. Thermoplast. Compos. Mater.*, **51**, 2631 (2017). <https://doi.org/10.1177/0021998316673894>.
55. G. Fredi, A. Dorigato, L. Fambri, and A. Pegoretti, *Compos. Sci. Technol.*, **158**, 101 (2018). <https://doi.org/10.1016/j.compscitech.2018.02.005>.
56. G. Fredi, A. Dorigato, and A. Pegoretti, *Express Polym. Lett.*, **12**, 349 (2018). <https://doi.org/10.3144/expresspolymlett.2018.30>.
57. A. Dorigato, G. Fredi, and A. Pegoretti, "9th International Conference on "Times of Polymers and Composites," in AIP Conference Proceedings, (2018).
58. G. Fredi, A. Dorigato, S. Unterberger, N. Artuso, and A. Pegoretti, *J. Appl. Polym. Sci.*, **136**, 47408 (2019). <https://doi.org/10.1002/app.47408>.
59. A. Dorigato, G. Fredi, and A. Pegoretti, *J. Appl. Polym. Sci.*, **136**, 47434 (2019). <https://doi.org/10.1002/app.47434>.
60. C. Dong and I.J. Davies, *Compos. B*, **72**, 65 (2015). <https://doi.org/10.1016/j.compositesb.2014.11.031>.
61. A. Jamekhorshid, S.M. Sadrameli, and M. Farid, *Renew. Sustain. Energy Rev.*, **31**, 531 (2014). <https://doi.org/10.1016/j.rser.2013.12.033>.
62. E.N. Brown, S.R. White, and N.R. Sottos, *J. Mater. Sci.*, **39**, 1703 (2004).
63. G. Gamon, P. Evon, and L. Rigal, *Ind. Crop Prod.*, **46**, 173 (2013). <https://doi.org/10.1016/j.indcrop.2013.01.026>.
64. I.D.G. Ary Subagia, Y. Kim, L.D. Tijing, C. Sang Kim, and H. Kyong Shon, *Compos. B*, **58**, 251 (2014). <https://doi.org/10.1016/j.compositesb.2013.10.027>.
65. M. Abdel Ghafaar, A.A. Mazen, and N.A. El-Mahallawy, *J. Eng. Sci.*, **34**, 453 (2006).